metals

MDPI

Article

Coexistence of Intermetallic Complexions and Bulk Particles in Grain Boundaries in the ZEK100 Alloy

Boris Straumal [1,2,*], Kristina Tsoy [1], Aleksandr Druzhinin [1], Valery Orlov [1], Natalya Khrapova [1], Gregory Davdian [1,2], Gregory Gerstein [3] and Alexander Straumal [4]

[1] Osipyan Institute of Solid State Physics of the Russian Academy of Sciences, Ac. Osipyan Str. 2, 142432 Chernogolovka, Russia; tsoy@issp.ac.ru (K.T.); druzhinin@issp.ac.ru (A.D.); orlov@issp.ac.ru (V.O.); khrapova@issp.ac.ru (N.K.); m155269@edu.misis.ru or faberest@yandex.ru (G.D.)
[2] Department of Physical Chemistry, National University of Science and Technology MISiS, Leninskiy Ave. 4, 119049 Moscow, Russia
[3] Institute for Material Science, Leibniz Universität Hannover, An der Universität 2, 30823 Garbsen, Germany; gerstein@iw.uni-hannover.de
[4] Department of Materials for Agrotechnology, Cotton Breeding, Seed Production and Agrotechnologies Research Institute, University Str. 3, Salar 702147, Uzbekistan; astraumal@umail.uz
* Correspondence: straumal@issp.ac.ru; Tel.: +7-916-676-8673

Abstract: Magnesium-based alloys are highly sought after in the industry due to their lightweight and reliable strength. However, the hexagonal crystal structure of magnesium results in the mechanical properties' anisotropy. This anisotropy is effectively addressed by alloying magnesium with elements like zirconium, zinc, and rare earth metals (REM). The addition of these elements promotes rapid seed formation, yielding small grains with a uniform orientation distribution, thereby reducing anisotropy. Despite these benefits, the formation of intermetallic phases (IP) containing Zn, Zr, and REM within the microstructure can be a concern. Some of these IP phases can be exceedingly hard and brittle, thus weakening the material by providing easy pathways for crack propagation along grain boundaries (GBs). This issue becomes particularly significant if intermetallic phases form continuous layers along the entire GB between two neighboring GB triple junctions, a phenomenon known as complete GB wetting. To mitigate the risks associated with complete GB wetting and prevent the weakening of the alloy's structure, understanding the potential occurrence of a GB wetting phase transition and how to control continuous GB layers of IP phases becomes crucial. In the investigation of a commercial magnesium alloy, ZEK100, the GB wetting phase transition (i.e., between complete and partial GB wetting) was successfully studied and confirmed. Notably, complete GB wetting was observed at temperatures near the liquidus point of the alloy. However, at lower temperatures, a coexistence of a nano-scaled precipitate film and bulk particles with nonzero contact angles within the same GB was observed. This insight into the wetting transition characteristics holds potential to expand the range of applications for the present alloy in the industry. By understanding and controlling GB wetting phenomena, the alloy's mechanical properties and structural integrity can be enhanced, paving the way for its wider utilization in various industrial applications.

Keywords: complexions; magnesium alloy; grain boundary; phases; transitions

Citation: Straumal, B.; Tsoy, K.; Druzhinin, A.; Orlov, V.; Khrapova, N.; Davdian, G.; Gerstein, G.; Straumal, A. Coexistence of Intermetallic Complexions and Bulk Particles in Grain Boundaries in the ZEK100 Alloy. *Metals* **2023**, *13*, 1407. https://doi.org/10.3390/met13081407

Academic Editor: Xiao-Wu Li

Received: 2 July 2023
Revised: 27 July 2023
Accepted: 4 August 2023
Published: 6 August 2023

1. Introduction

The investigation of magnesium-based alloys has gained significant popularity in modern materials science [1–4]. The interest in these alloys is evident due to their widespread use in technologically demanding industries. They are highly valued for their lightweight nature, relatively good strength, and toughness. However, despite their high demand, there is still room for improvement in their properties.

One notable challenge arises from magnesium's hexagonal unit cell, which results in fewer dislocation slip systems compared to metals with face-centered cubic (fcc) or

body-centered cubic (bcc) crystal structures. This limitation leads to reduced formability and increased brittleness. To address this issue, numerous investigation and development projects are dedicated to enhancing the properties of magnesium-based alloys. One of the primary approaches to achieving this goal is through alloying with elements such as zirconium, zinc, and rare earth metals (REM). These elements induce seed formation during crystallization, thereby reducing the grain size and promoting a more uniform spatial distribution of basal plane orientations within the magnesium grains [1,2,5–8].

The REM-doped Mg-based alloys exhibit distinct behaviors compared to conventional alloys, particularly in terms of anisotropy and strain rate sensitivity [9]. Unlike traditional rolled AZ31 Mg alloys, which possess a strong texture [10], ZEK100 Mg alloy sheets display a weak texture [10–14]. The ZEK100 alloy typically contains 1.3wt.% Zn, 0.2wt.% Nd, 0.25wt.% Zr, and 0.01wt.% Mn [15].

Extensive research has been conducted on the mechanical properties of the ZEK100 alloy, including studies on damage and fracture [16–18], warm and hot deformation behavior [19,20], propagative plastic instabilities [21], plastic strain heterogeneity [22], tension–compression yield asymmetry [23], as well as details of extrusion [24,25], hot rolling [26], warm forming [27], cyclic deformation, fatigue, and anelasticity [28–33]. To characterize the properties of ZEK100, plane strain bending using the V-bend test [34] and a three-point bending test [35] were employed. Furthermore, limit-forming diagrams were constructed [36–38], twin banding was modeled [39], and constitutive plasticity models were developed [40–46] to predict and explain the mechanical behavior of the alloy.

ZEK100 is extensively utilized as a biodegradable material for prostheses and implants [47–62], especially those requiring improved mechanical properties [47,63] and controlled corrosion behavior [64–71]. Additionally, it finds applications as myocardial stabilizing structures [56,57,72] and as wire reinforcement in phosphate cement composites for load-bearing bone replacements [61,73]. In the production of components from the ZEK100 alloy, advanced treatment methods are employed. These include ultrasonic spot welding [74–78], friction stir spot welding [79–81], laser welding/brazing [82], and electropulse treatment [83]. These methods ensure the fabrication of high-quality parts with desirable characteristics.

The modification of magnesium has led to new and unfamiliar challenges. When alloying elements are introduced, they can create precipitates localized on defects, especially at grain boundaries (GBs). The rare earth metals can form hard intermetallic compounds with magnesium. While these precipitates enhance the material's strength, they can also introduce brittleness, particularly when GBs are replaced by continuous layers of intermetallic compounds. Under deformation, cracks may propagate along these brittle layers of a secondary phase, even if the magnesium grains themselves are more ductile. To anticipate and address such situations, it becomes crucial to study phase transitions that can alter the morphology of GB phases and precipitates in polycrystalline multiphase magnesium alloys. Understanding the formation or disintegration of GB layers with second phases and their impact on material properties is particularly vital for developing new alloys and expanding the range of applications for existing ones.

Surface phase transitions were initially proposed as a theoretical concept by Cahn and Ebner [84,85]. They highlighted that phase transitions are not restricted to three-dimensional systems but can also occur on two-dimensional boundaries and surfaces, both internal and external. These surfaces may undergo structural and shape changes (faceting, complexion formation) [86,87], a redistribution of adsorbed alloying elements (pre-melting, complexion formation) [88,89], or even a redistribution of bulk secondary phases situated on the surface (wetting) [90,91]. Over the years, the concept of wetting has been demonstrated for external surfaces and individual grain boundaries (GBs) [89,92], as well as for ensembles of GBs [89–91,93]. Such surface phase transitions are based on the disparity in surface tension energies between the GBs and the interphase boundaries, and these can change with varying system conditions like temperature or pressure [94,95]. The equilibrium of this process is described by Young's formula, which provides the contact

angle θ at the intersection of two interphase boundaries with the energy σ_{IB} and a GB with the energy σ_{GB}, as follows:

$$\sigma_{GB} = 2\sigma_{IB} \cos \theta. \quad (1)$$

If the difference between the energy values of two interphase boundaries, $2\sigma_{IB}$, and the σ_{GB} energy decreases, the contact angle θ will also decrease. When the energy of two interfaces, $2\sigma_{IB}$, becomes equal to the GB energy, σ_{GB} ($2\sigma_{IB} = \sigma_{GB}$), the contact angle becomes zero (θ = 0). At this point, the system replaces the GB with a layer of the secondary phase confined between two interphase boundaries. This phenomenon is referred to as the wetting GB transition. The temperature at which the surface energies become equal ($2\sigma_{IB} = \sigma_{GB}$) and the contact angle becomes zero (θ = 0), denoted by T_w, is known as the wetting temperature of the GB. Each GB may have a different structure and, consequently, different σ_{GB} values. As a result, different GBs associated with the same secondary phase will have distinct wetting temperatures (T_w). A polycrystal will exhibit a range of T_w values, reflecting the diverse spectrum of GBs present within it. The spectrum of GBs, in turn, is influenced by the manufacturing method and processing used to produce the respective polycrystalline sample. These factors play a crucial role in determining the properties and behavior of the material.

Our previous investigations have primarily focused on the EZ33A alloy, revealing the presence of GB wetting phase transitions involving second liquid and solid phases at various temperatures [3,4,96]. The EZ33A is a widely used magnesium casting alloy in the industry, particularly for manufacturing bulk parts like differentials' housings. However, a significant issue with this alloy arises from the tendency of its alloying elements to form brittle intermetallic compounds within grain boundaries, rendering the GBs themselves brittle. These phases are commonly referred to as the *T*-phase or Mg_{12}(RE) intermetallic compound in the literature. Consequently, producing thin parts from this alloy poses challenges, as they lack adequate strength and toughness due to the propagation of cracks along the brittle secondary phases in GBs.

Studies [3,4,96] have revealed that just above the solidus temperature, at 530 °C, more than 10% of the GBs in EZ33A are already completely wetted by the bulk liquid phase. As the temperature rises, the fraction of wetted GBs gradually increases, reaching 85% at 580 °C. However, at this temperature, the fraction of wetted GBs seems to saturate, which could be attributed to experimental errors during quenching from elevated temperatures or the presence of GBs with low misorientation angles and/or coincidence site lattice GBs in the material. These GBs have lower σ_{GB} energies and might remain unwetted in the alloy until the melting temperature is reached. Leveraging their understanding of the GB wetting phase transition in the EZ33A alloy, the authors proposed a heat treatment method to reduce the number of wetted GBs and thereby enhance the ductility of the alloy [3,4].

The focus of this study is the investigation of GB phase transitions in the ZEK100 alloy, which is another significant magnesium-based alloy [9–83]. The ZEK100 alloy shares similar alloying elements with EZ33A, albeit at lower concentrations [3]. Consequently, it is reasonable to anticipate a substantial difference in the structure and morphology of ZEK100, primarily due to the reduced volume of the secondary phase present in its GBs. The primary objective of this research is to determine whether wetting of the GBs will occur in the ZEK100 alloy and to understand how it differs from the wetting transition observed in the EZ33A alloy. By exploring these wetting phenomena, we aim to gain valuable insights into the behavior and characteristics of the ZEK100 alloy, contributing to a better understanding of its properties and potential applications.

2. Materials and Methods

The nominal composition of the ZEK100 alloy is 1 wt.% zinc, 0.1 wt.% zirconium, 0.1 wt.% rare earth metals (neodymium, yttrium, cerium, and lanthanum), with the remaining balance being magnesium. The alloy was produced at the Institute for Material Science of Leibniz University in Hannover, Germany, using a special induction oven equipped with two crucibles and magnetic stirring. To obtain samples for analysis, the ZEK100 ingot was

cut into 6 × 6 × 12 mm pieces using the electro-erosion method. The samples underwent a thorough cleaning process involving an ultrasonic bath with acetone, followed by etching in a 75% HCl + 25% H_2O solution to remove any contaminants and oxide films. Subsequently, the cleaned samples were placed in evacuated quartz ampoules with a residual Ar pressure of 200 mbar to protect the magnesium alloy from oxidation and any potential reactions with contaminants during high-temperature treatment.

To investigate the influence of GB phase transitions on the microstructure of the ZEK100 alloy, the ampoules containing the samples were annealed at various elevated temperatures ranging from 500 to 640 °C to achieve a stable structure. During this annealing process, the presence of a liquid phase was observed in the samples between 500 and 640 °C. After the annealing step, the ampoules were rapidly quenched in liquid nitrogen, simultaneously breaking the ampoules to achieve a high cooling rate.

The temperature range for this study was selected with great care. It was chosen to specifically investigate the wetting of grain boundaries by the second liquid phase and to experimentally determine both the solidus and liquidus temperatures for the ZEK100 alloy. Through these systematic investigations, our goal is to develop a comprehensive understanding of the behavior and phase transitions occurring within the ZEK100 alloy. By doing so, we can gain valuable insights into its material properties and explore its potential applications.

The method of quenching in liquid nitrogen with a simultaneous breaking of the ampoule was carefully selected for specific reasons. While water quenching offers a much higher quenching rate compared to liquid nitrogen, the latter was chosen due to the unique characteristics of magnesium samples. When quenching in water, magnesium's reactivity with oxygen can lead to combustion, making it unsuitable for this material.

To address this issue, the samples were sealed in evacuated quartz ampoules with an argon atmosphere inside. Quenching the ampoules in water without breaking them would cause the heat to escape through the argon, which has a lower thermal conductivity (0.015 W/(m × K) at standard conditions) compared to nitrogen. Consequently, the argon acts as a thermal insulator during the quenching process, resulting in a significantly lower quenching rate, approximately forty times slower than direct water quenching or even slower due to low argon pressure (200 mbar or less). Additionally, quenching through the corners of the sample, resting on the curved cylindrical ampoule walls, could create localized and varying cooling rates across the sample, leading to different microstructures. Such discrepancies would introduce substantial errors into the experiment, which is not acceptable. Considering all these factors, quenching in liquid nitrogen with ampoule breaking was deemed the most suitable approach to achieve the desired high cooling rate uniformly across the sample, enabling reliable and accurate investigations of the GB phase transitions in the ZEK100 alloy.

On the other hand, quenching in liquid nitrogen offers several advantages. As the ampoule is broken beneath the surface of the liquid nitrogen, the red-hot sample remains completely shielded from any contact with oxygen or moisture. Unlike the water quenching setup, where cooling occurs through two angles of the sample, quenching in liquid nitrogen ensures cooling across the entire surface of the sample. Although gaseous nitrogen has a thermal conductivity of 0.033 W/(m × K), it still exceeds the thermal conductivity of argon. Consequently, the cooling rate in a continuous gas layer of nitrogen is approximately twice as fast as quenching in an unbroken ampoule submerged in water. Additionally, the evaporation of nitrogen on the sample's surface, the growth of bubbles, and the subsequent detachment of these bubbles further aid in dissipating heat from the sample. This additional heat dissipation mechanism significantly enhances the overall quenching rate compared to quenching in an intact ampoule, further boosting the efficiency of the process.

The samples were prepared by embedding them in metallographic conductive resin, followed by grinding with SiC paper and polishing with diamond paste to achieve a surface finish of 0.25 µm. The investigation of the structural changes after annealing was carried out using the Versa 3D Dual beam scanning electron microscope (SEM) from FEI (Hillsboro,

OR, USA). The SEM was equipped with a secondary electron detector (SE2), a backscatter electron detector (BSE), and an energy-dispersive X-ray spectroscopy (EDX) detector.

The SE2 contrast allowed us to examine the surface topography of the samples and attain the best focus for analysis. Meanwhile, the BSE provided the highest elemental contrast, enabling the visualization of precipitates and distinct differentiation between individual magnesium grains. Utilizing the EDX method, we could evaluate the element concentration in different phases and estimate the total number of co-existing phases within the samples. These advanced microscopy and spectroscopy techniques were crucial for conducting a comprehensive investigation of the microstructural changes and elemental compositions in the ZEK100 alloy after annealing, offering valuable insights into its phase transitions and overall material behavior.

The wetting state of the grain boundaries (GBs) was assessed through the examination of the wetting phase's morphology. A GB was considered to be completely wetted if the wetting phase was present in both GB triple junctions at the ends of the GB and formed a continuous layer extending from one triple junction to the other. On the contrary, if the wetting phase formed a discontinuous layer or if it existed as a uniaxial particle along the GB, then the GB was classified as not wetted. These criteria were used to determine the wetting status of the GBs in the samples, providing valuable information about the extent of GB wetting and its impact on the microstructure of the ZEK100 alloy.

3. Results and Discussion

The initial structure of the as-cast ZEK100 alloy was thoroughly examined. Figure 1 illustrates the typical morphology of this state, which consists of the Mg-based solid solution (referred to as (Mg)). The (Mg) grains exhibit a uniaxial structure and appear as dark grey regions in the SEM micrograph, with some lighter grey areas enriched in alloying elements like Zr. The average grain size of the magnesium grains (Mg) is approximately 210 μm, while the size of the enriched areas is about 70 μm (as seen in Figure 2).

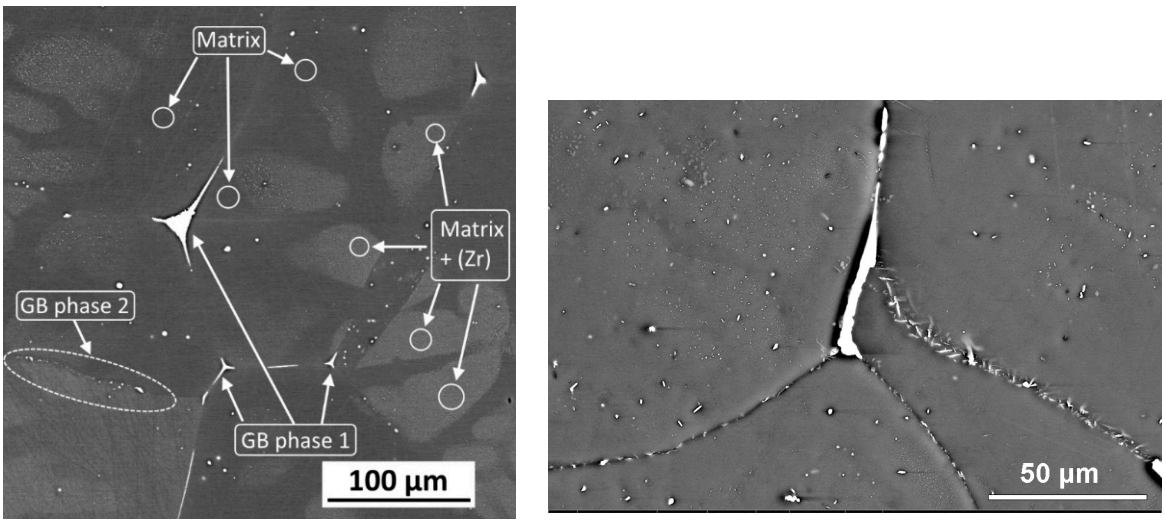

Figure 1. SEM micrographs of the as-cast ZEK100 alloy. (**a**) The dark-grey areas correspond to the (Mg) grains, while the bright-grey areas represent (Mg) regions enriched with Zr, as indicated by white circles. The elongated particles situated at the grain boundaries are classified into two types: bright white particles (phase 1), shown by arrows, and bright grey particles (phase 2), marked by dotted ellipse. Additionally, in Figure (**b**), two grain boundary (GB) triple junctions are shown: the top GB contains a continuous layer of the bright white phase 1, and the bottom three GBs exhibit needles of the bright grey phase 2. Furthermore, small round precipitates in the bulk of the (Mg) matrix can also be observed.

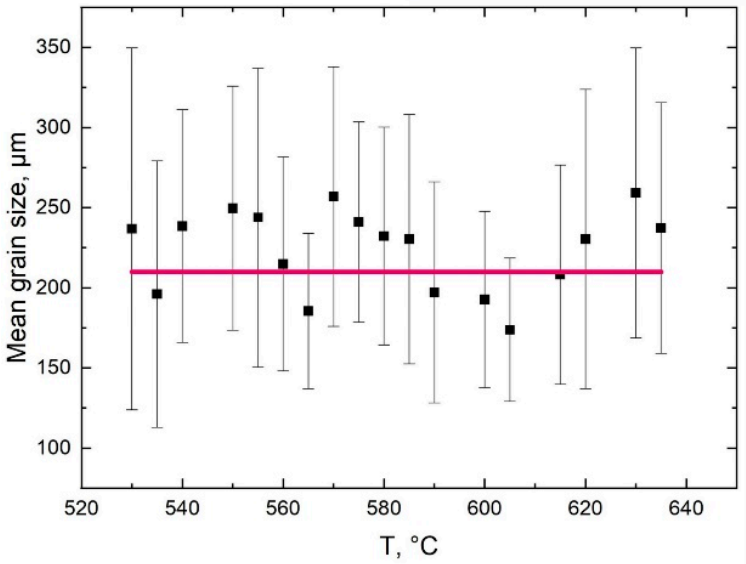

Figure 2. The mean size of (Mg) grains measured at various temperatures. It is almost temperature-independent (see the red line).

In addition to the (Mg) grains, there are other phases present in the structure, distinguishable as bright white (phase 1) or bright grey (phase 2). These phases are situated at the grain boundaries of the (Mg) grains and can be categorized into two types. The first type, denoted as GB phase 1, comprises the majority of the particles located at the (Mg)/(Mg) grain boundaries. These GB phase 1 particles are relatively large, often elongated, and can either have a lenticular shape or form long continuous layers that replace the grain boundaries. They can also appear as uniaxial particles at the (Mg)/(Mg) grain boundary triple junctions. On average, their thickness measures around 4.6 μm for layers and lenses on the (Mg)/(Mg) grain boundaries, and their diameter is approximately 6 μm for the uniaxial particles. The surface area fraction covered by this phase in the initial sample amounts to 0.8%. Overall, these detailed observations provide crucial insights into the microstructure of the as-cast ZEK100 alloy, setting the foundation for further investigations and analyses.

The X-ray diffraction (XRD) patterns of the samples annealed at 530 °C and 550 °C are presented in Figure 3a,b, respectively. These patterns exhibit only the characteristic lines of the (Mg) matrix, indicating that the total amount of secondary phases falls below the sensitivity limit of the XRD method (i.e., below 1–2 vol.%). Notably, there is a distinct variation in the intensity distribution between different (Mg) peaks in Figure 3a,b, indicating a certain change in texture above 530 °C. Similar XRD patterns are observed for annealings at 540–610 °C, resembling Figure 3b. Consequently, the volume fraction of GB phases 1 and 2 is so minute that none of the XRD investigations could identify them in the diffraction patterns of the magnesium matrix (Mg) (as depicted in Figure 3). To conduct a quantitative analysis, surface fraction values were derived from SEM micrographs of the sample sections, revealing the sample's structural composition. A very small volume of the structure (approximately 0.1%) is occupied by particles of the second phase (GB phase 2). These particles are primarily located within the GBs, as shown in Figure 1b, although they can sometimes be found within the grains as well. These particles are small and uniformly possess a uniaxial round shape, with an average size of around 400 nm.

It is highly likely that the particles are formed by distinct phases since they are occasionally found to co-exist on the same (Mg)/(Mg) grain boundaries in close proximity. However, a noticeable difference in their shapes is observed, with GB phase 2 displaying a round shape and GB phase 1 exhibiting a lenticular shape. These distinct shapes imply variations in the energies of the interphase boundaries between the matrix phase and GB phases 1 and 2. Such a conclusion can be readily drawn from Young's Formula (1).

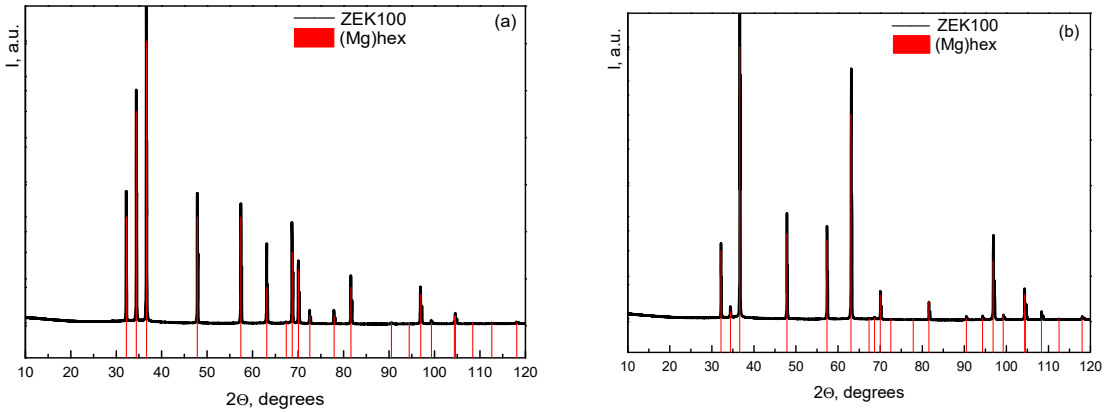

Figure 3. XRD patterns of the ZEK 100 samples annealed at 530 °C (**a**) and at 550 °C (**b**). The positions of hcp-Mg peaks are shown by the vertical red lines.

The conclusion regarding the presence of two different grain boundary (GB) phases was further supported by EDX measurements of the chemical composition of all identified phases. The compositions of these observed phases are presented in Table 1. Phase 1 shows an enrichment of Zn, Ce, and La, whereas Phase 2 is enriched with Zn, Zr, and Y. It is essential to consider the limitations of EDX analysis when interpreting the chemical composition values. The reaction volume responsible for generating the X-ray signal under the bombardment of the primary electron beam has a diameter of about 0.5 to 1 µm and a depth of up to 500 nm, depending on the material and SEM settings. Consequently, precise chemical composition values for a particular phase should not be assumed unless the particle of the investigated phase significantly exceeds the volume from which the X-ray signal is collected. Despite this limitation, the EDS measurements of the GB phases in this study provide us with qualitative data for their composition, confirming the existence of differences in the phase composition of GB phases 1 and 2. Additionally, it is crucial to remember that the error of EDX measurements is approximately 0.1 wt.%. The error values presented in Table 1 are generated using the EDX software EDAX APEX 1.1 and indicate the reliability of each identified concentration.

Table 1. Chemical composition of structural components of the ZEK100 alloy.

Concentration of Elements, wt.%	Matrix	Matrix + (Zr)	GB Phase 1	GB Phase 2
Mg	97.71 ± 0.02	98.43 ± 0.02	73.31 ± 0.13	79.59 ± 0.123
Zn	1.12 ± 0.08	0.98 ± 0.09	10.38 ± 0.26	3.96 ± 0.49
Zr	0.01 ± 0.07	0.14 ± 0.07	0.34 ± 0.2	13.17 ± 0.7
Ce	0.12 ± 0.1	0.1 ± 0.11	6.873 ± 0.29	0.36 ± 0.66
Nd	0.02 ± 0.11	0.08 ± 0.11	0.91 ± 0.5	0.18 ± 0.8
Y	0.03 ± 0.07	0.06 ± 0.02	0.19 ± 0.19	2.32 ± 0.37
La	0.15 ± 0.1	0.19 ± 0.1	7.76 ± 0.29	0.42 ± 0.63

We observe that the matrix phase (Mg) consists mainly of pure magnesium with a minor zinc content. The bright areas within the (Mg) solid solution exhibit an enrichment of zirconium, leading to the formation of needle-shaped particles that are nearly pure zirconium. Figure 4 illustrates a typical image of these needles, which can have a thickness of up to 500 nm and a length ranging from 5 to 10 µm. Remarkably, these needles possess a hexagonal cross-section. The grain boundaries (GBs) are adorned with particles of GB phase 1, characterized by an enrichment of Zn, Ce, and La. It is reasonable to assume that these particles belong to the intermetallic compound Mg_{12}(RE), where RE represents rare earth metals [2,6]. On the other hand, GB phase 2 is enriched in zinc, zirconium, and yttrium.

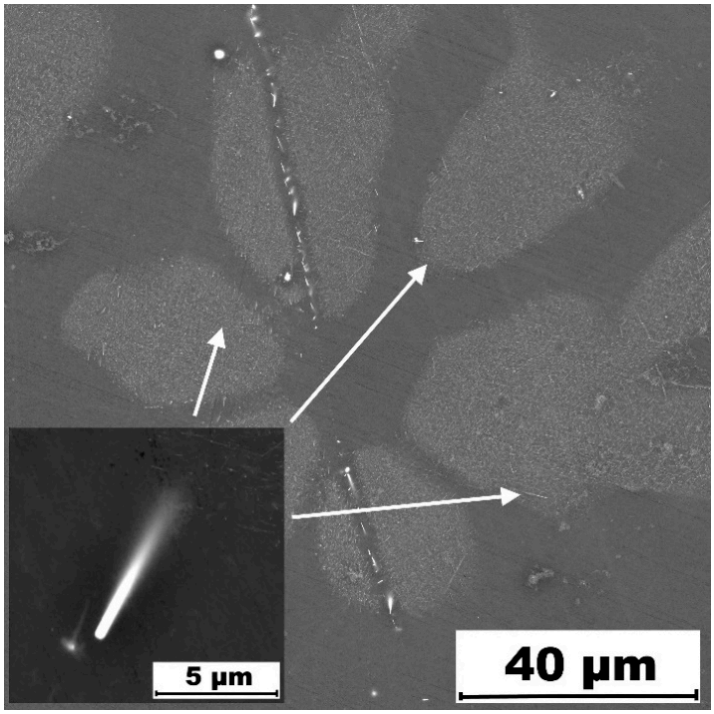

Figure 4. SEM micrograph of as-cast ZEK100 alloy. Zirconium enrichment in the magnesium grains. Needle-shaped Zr-rich particles are clearly seen (shown by the arrows).

After anneals at high temperature, the microstructure of the samples changed significantly. Figure 5 shows an example how the surface tension energy balance can influence the morphology of the precipitates.

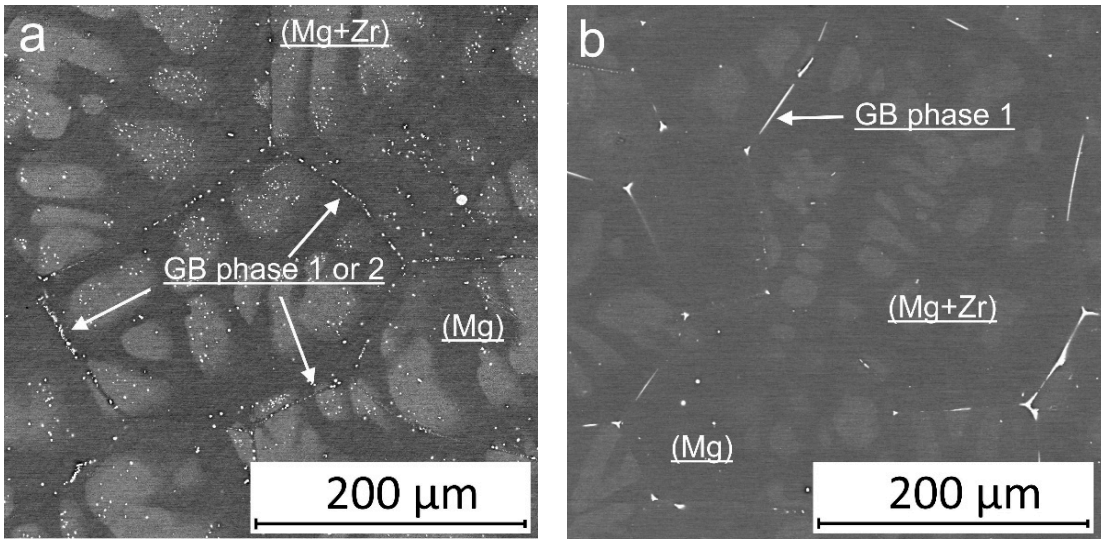

Figure 5. SEM micrographs of the ZEK100 alloy after a 2 h anneal at (**a**) 530 °C and (**b**) 590 °C.

By comparing the initial and annealed structures of the samples, the solidus temperature T_{sol} of the ZEK100 alloy was determined. The solidus temperature T_{sol} is defined as the temperature range where the resulting structure remains unchanged from the initial structure at the highest annealing temperature, and it starts to differ from the initial structure at the lowest annealing temperature. Figure 5a illustrates the structure after annealing at 530 °C. It is evident that after 2 h of annealing at 530 °C, the GB phases in the ZEK100 alloy underwent significant changes in shape compared to the initial as-cast state

(as depicted in Figure 1). This observation suggests that the GB phases were in a liquid state at the annealing temperature. The solidus temperature (T_{sol}) was determined to be approximately 525 ± 5 °C, as this is the temperature at which the first portion of the phases in the GBs started to melt. Complete melting of the material occurred at around 645 ± 5 °C, which corresponds to the liquidus temperature (T_{liq}).

Following a 2 h annealing at different temperatures, the mean size of (Mg) grains remained almost unchanged up to 600 °C. Subsequently, it increased to 210 µm and remained stable at 210–220 µm up to 620 °C (as shown in Figure 2). At 630 °C, the mean grain size further grew to 260–270 µm. Beyond this point, it became impractical to measure the mean grain size at higher temperatures due to the rapid growth of the liquid phase. At 640 °C, the remaining solid grains were surrounded by a pool of liquid, resulting in the complete wetting of all grain boundaries [97]. Consequently, it became impossible to ascertain the role of grain boundary wetting in the formation of such structures. Notably, at elevated temperatures, the Mg-rich grains did not undergo significant growth (as observed in Figure 2), indicating that the matrix grain structure and the spectrum of GB types remained largely unchanged. Consequently, any alterations in mechanical or diffusion properties within the material are attributed to the rearrangement of GB phases, driven by changes in the GB energy (σ_{GB}). These findings provide experimental evidence for the crucial role of GB phase transitions as an independent factor in structure formation. Importantly, these GB phase transitions can occur independently of grain growth or bulk phase transformations.

Furthermore, it is evident that while the (Mg) grains did not experience significant growth, the morphology of GB phase particles underwent a drastic change across the range of annealing temperatures. As shown in Figure 5a, after the heat treatment, the GB phase 1 (the REM-enriched one) fragmented into numerous small droplets (particles) along the grain boundary. From the perspective of Young's Formula (1), we can infer that in this state, the GB energies (σ_{GB}) are lower than the interphase boundary energies ($2\sigma_{IB}$). Consequently, the system tends to minimize the surface area of such boundaries. As known from geometry, a sphere exhibits the smallest surface area compared to other shapes. Within the context of the GB wetting theory, the spherical shape of GB phases represents a state with no GB wetting.

As the annealing temperature increases, the morphology of the GB droplets (particles) undergoes a gradual transformation. In Figure 5b, we observe the microstructure of a sample annealed at 590 °C. The GB phase 1 (the REM-enriched one) changes its shape from round droplets to elongated lenses and flat layers, forming connections between triple junctions filled with the same phase. Notably, it is essential to highlight that GB phase 1 not only wets the (Mg)/(Mg) grain boundaries but also fills all visible triple junctions of (Mg) grains. This observation suggests that, similar to what was previously noted in Al-based alloys and the EZ33A alloy, the GB triple junctions become entirely wetted by the melt before the grain boundaries [96,98–100]. On the other hand, the GB phase 2 (enriched with Zn and Zr) appears to have dissolved into the surrounding phases, with no small particles visible in the grain boundaries. The combined area fraction of both GB phases in the micrographs of this structure was approximately 0.7%. This finding suggests that the ZEK100 alloy was close to the solidus line. Assuming that GB phase 2 completely wets all (Mg)/(Mg) grain boundaries, its layer thickness within the grain boundaries would range from about 0.5 to 1 µm. Consequently, this makes it an excellent candidate for investigating GB phase transitions. Moreover, the observation that the GB phase 1 (the RE-enriched one) forms uniform layers in (Mg)/(Mg) grain boundaries at elevated temperatures confirms that, akin to EZ33A [3], a GB wetting phase transition occurs on the (Mg)/(Mg) grain boundaries in the ZEK100 alloy.

In an attempt to provide an explanation for the observed differences, a more detailed SEM investigation was conducted. The examination of seemingly "clean" (Mg)/(Mg) grain boundaries, devoid of impurities, yielded an unexpected and astonishing discovery. In some of these (Mg)/(Mg) grain boundaries, extremely thin, bright-grey lines were

identified, indicating the presence of a very thin layer enriched in alloying elements. The imaging was carried out using backscatter electron contrast (BSE) at magnifications ranging from 20,000 to 40,000 with exceptionally high contrast levels. The first sample where these thin GB layers were detected underwent annealing at 610 °C. To confirm that these GB lines resulted from a high concentration of alloying elements in the grain boundary and were not a metallographic artifact, a comparison of one region of the sample was performed using two different contrast regimes. This verification process served to validate the authenticity of the thin GB layers and their association with a substantial presence of alloying elements in the grain boundary.

Figure 6 presents the results of this comparison. The first contrast type used is the secondary electron contrast (SE2). SE2 only detects electrons that are emitted when primary electron beam knocks them out from their orbits in the atoms of the alloy. However, since knocking out an electron requires a significant amount of energy, this process occurs primarily in a thin surface layer of the sample, where electrons from the electron beam have not yet lost much energy due to scattering. As a result, the SE2 signal provides a picture of the surface texture of the sample and does not offer substantial information about its internal structure.

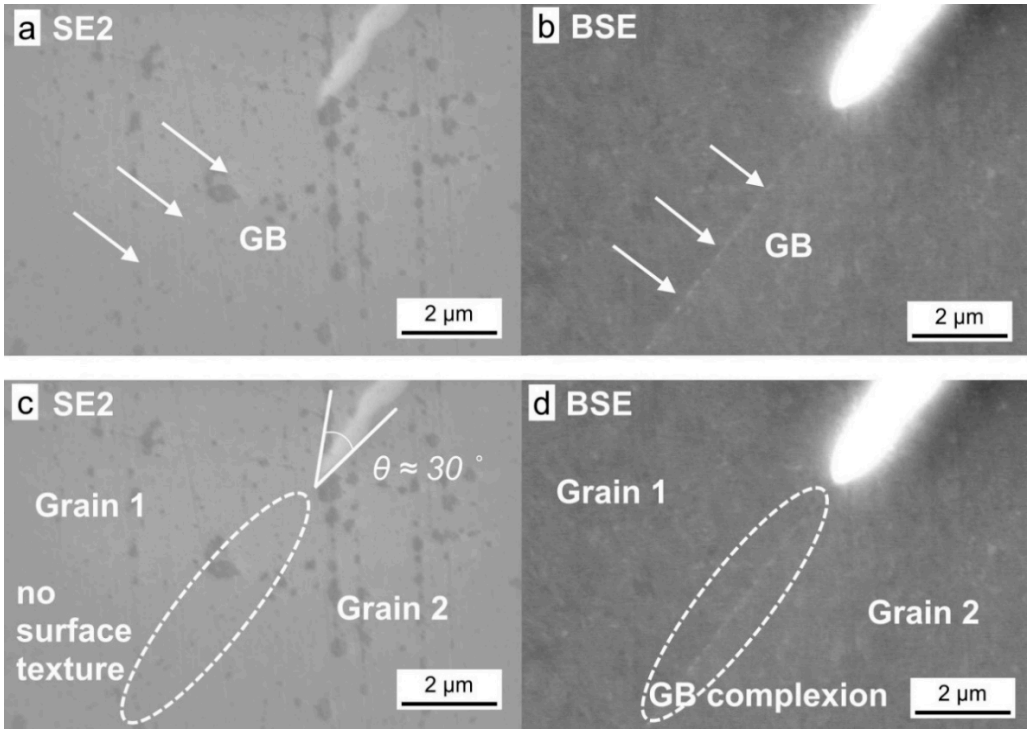

Figure 6. SEM micrographs of ZEK100 sample after annealing at 610 °C. (**a**) (Mg)/(Mg) GB with a particle of a second phase (enriched by Zn and Zr) in the SE2 contrast. The location of the (enriched by Zn and Zr) GB is shown by white arrows. (**b**) GB with a particle of a second phase in the BSE contrast. The location of the (enriched by Zn and Zr) GB is shown by white arrows. A thin bright line is to be seen on the GB. (**c**) and (**d**) the same places as (**a**) and (**b**), respectively. The GB location and the presence of a GB complexion is highlighted by a white dotted ellipse.

In Figure 6a,c, the SE2 contrast primarily reveals surface features. The dark spots observed are traces of oxidation, which are inevitable as a well-polished magnesium surface is highly reactive and prone to oxidation. On the other hand, the bright grey particle corresponds to a bulk particle of GB phase 1 (the REM-enriched one). No thin lines or anything similar are visible in the SE2 images, indicating that the observed phenomenon is not a surface feature. However, using the backscatter electron contrast (BSE) imaging in Figure 6b,d, we were able to visualize that the seemingly empty (Mg)/(Mg) grain boundary

actually contains trace amounts of alloying metals. These metals have a significantly higher atomic weight than magnesium and, as a result, scatter back many more electrons than Mg atoms. Determining the exact thickness of the GB layer solely based on the BSE images is challenging. Nevertheless, the approximate thickness of the layer falls within the range of 10 to 100 nm. According to [101], this corresponds to a nanolayer GB complexion. The coexistence of a GB complexion and a bulk particle of GB phase with a non-zero contact angle is a unique observation not previously recorded in any magnesium-based alloys. This configuration of segregation and the second phase on the GB is classified in the literature as pseudo partial wetting [102–105]. It has been reported previously only in the NdFeB, Al-Zn, and WC-Co systems.

Upon the discovery of these thin layers (complexions) in (Mg)/(Mg) grain boundaries in the sample annealed at 610 °C, all other samples were also investigated. Similar layers were found in samples annealed at temperatures ranging from 530 °C to 620 °C, with the fraction of such grain boundaries varying from 10% to 30% of all GBs. Notably, these complexions often coexisted with bulk particles of GB phase 1, characterized by a non-zero contact angle. This coexistence suggests the existence of an equilibrium of surface tension energies between the complexions and the bulk GB phase. However, the EDX method lacks the precision required to visualize, or even provide an estimate of, the elements present in these complexions. As a result, the question of whether the complexions and the bulk GB phase are the same or different remains unanswered. To explain this coexistence of thin complexions in the GBs and bulk particles of the second phase with a non-zero contact angle, further investigations are warranted. Transmission electron microscopy (TEM) is a suitable technique for measuring the small thickness, chemical composition, and crystal structure of the complexions. Additionally, TEM would offer insights into the chemical composition and distribution of elements in the bulk particles. This analysis would allow us to confirm or refute the assumption that both the complexions and the bulk particles have the same composition. If the compositions are equal, then the existence of the pseudo partial wetting state would be established. However, if the compositions are different, it could indicate that the liquid phase on the grain boundaries at elevated temperatures is non-uniform, and the complexion may be formed by GB phase 2 or another scarce phase that arises during the experiment's temperature conditions. In such a scenario, the partial wetting state of GBs would align well with the modern understanding of the mechanisms involved in complexion formation.

If the bulk and GB phases indeed turn out to be different, the current findings offer another intriguing conclusion. The thin complexion appears to function not as a distinct phase but rather as a two-dimensional film that alters the characteristics of the GB [106–108]. Rather than envisioning it as a phase with two limiting interphase boundaries, it is better understood as a GB with a modified energy value. At temperatures above the solidus line but below the liquidus line, the GB would typically possess high energy, leading to the initiation of the GB wetting transition. However, the presence of complexions modifies this energy landscape, reducing the GB's energy and making the wetting transition less favorable [106–108]. In this scenario, GB phase 1 would assume the shape of small spheres, as seen in Figure 5a. In essence, the formation of complexions representing a third phase may hinder the wetting transition by the second phase, effectively raising the wetting temperatures. This insight suggests that the interaction between complexions and GB phases plays a critical role in influencing the overall behavior of grain boundaries in the alloy.

4. Conclusions

The findings from the investigation of GB wetting phase transitions in the commercial magnesium alloy ZEK100 have been documented. The presence of a phase transition in (Mg)/(Mg) grain boundaries has been conclusively confirmed. Notably, the wetting of (Mg)/(Mg) grain boundaries was observed at temperatures near the melting point of the ZEK100 alloy, which corresponds to the liquidus temperature. The solidus temperature

for this alloy was determined to be 525 ± 5 °C, while the liquidus temperature was found to be 645 ± 5 °C. Moreover, the research into the GB phase morphology revealed a remarkable coexistence of a nano-scaled precipitate film, or complexion, along with bulk particles of the precipitate displaying non-zero contact angles. Two potential scenarios were proposed to explain this phenomenon. One possibility is the occurrence of pseudo-partial wetting in this system, while the other suggests a competition of GB wetting transitions driven by different phases. Remarkably, both of these scenarios have not been previously reported in magnesium alloys, underscoring the novel and intriguing nature of the observed phenomena in the ZEK100 alloy.

Author Contributions: Conceptualization, A.S. and G.G.; methodology, G.D., A.S., N.K. and K.T.; validation, V.O., A.D., N.K., K.T. and G.G.; formal analysis, G.D., N.K. and V.O.; investigation, K.T., N.K. and G.D.; resources, B.S. and G.G.; data curation, G.D. and A.S.; writing—original draft preparation, B.S. and A.S.; writing—review and editing, B.S. and G.G.; visualization, A.D.; supervision, A.S.; project administration, A.D.; funding acquisition, A.S. All authors have read and agreed to the published version of the manuscript.

Funding: This research received no external funding.

Institutional Review Board Statement: Not applicable.

Informed Consent Statement: Not applicable.

Data Availability Statement: Not applicable.

Acknowledgments: The authors are incredibly grateful for the technical support of Michail Yuskov.

Conflicts of Interest: The authors declare no conflict of interest.

References

1. Bryła, K.; Krystian, M.; Horky, J.; Mingler, B.; Mroczka, K.; Kurtyka, P.; Lityńska-Dobrzyńska, L. Improvement of Strength and Ductility of an EZ Magnesium Alloy by Applying Two Different ECAP Concepts to Processable Initial States. *Mater. Sci. Eng. A* **2018**, *737*, 318–327. [CrossRef]
2. Bryła, K.; Morgiel, J.; Faryna, M.; Edalati, K.; Horita, Z. Effect of High-Pressure Torsion on Grain Refinement, Strength Enhancement and Uniform Ductility of EZ Magnesium Alloy. *Mater. Lett.* **2018**, *212*, 323–326. [CrossRef]
3. Straumal, A.B.; Tsoy, K.V.; Mazilkin, I.A.; Nekrasov, A.N.; Bryła, K. Grain Boundary Wetting and Material Performance in an Industrial EZ33a Mg Cast Alloy. *Arch. Metall. Mater.* **2019**, *64*, 869–873. [CrossRef]
4. Straumal, A.; Mazilkin, I.; Tzoy, K.; Straumal, B.; Bryła, K.; Baranchikov, A.; Eggeler, G. Bulk and Surface Low Temperature Phase Transitions in the Mg-Alloy EZ33A. *Metals* **2020**, *10*, 1127. [CrossRef]
5. Trang, T.T.T.; Zhang, J.H.; Kim, J.H.; Zargaran, A.; Hwang, J.H.; Suh, B.C.; Kim, N.J. Designing a Magnesium Alloy with High Strength and High Formability. *Nat. Commun.* **2018**, *9*, 2522. [CrossRef]
6. Oshida, Y. *Magnesium Materials. From Mountain Bikes to Degradable Bone Grafts*; De Gruyter Publishing: Berlin, Germany, 2021; p. 808. [CrossRef]
7. Atrens, A.; Dietzel, W.; Srinivasan, P.B.; Winzer, N.; Kannan, M.B. Chapter 9: Stress Corrosion Cracking (SCC) of Magnesium Alloys. In *Stress Corrosion Cracking: Theory and Practice*; Woodhead Publishing: Cambridge, UK, 2011; pp. 341–380. [CrossRef]
8. Martinez, D.C.; Dobkowska, A.; Marek, R.; Cwieka, H.; Jaroszewicz, J.; Plocinski, T.P.; Donik, C.; Helmholz, H.; Luthringer-Feyerabend, B.; Zeller-Plumhoff, B.; et al. In vitro and in vivo Degradation Behavior of Mg-0.45Zn-0.45Ca (ZX00) Screws for Orthopedic Applications. *Bioact. Mat.* **2023**, *28*, 132–154. [CrossRef] [PubMed]
9. Wang, H.; Sun, X.; Kurukuri, S.; Worswick, M.J.; Li, D.Y.; Peng, Y.H.; Wu, P.D. The Strain Rate Sensitive and Anisotropic Behavior of Rare-Earth Magnesium Alloy ZEK100 Sheet. *J. Magn. Alloys* **2023**, *11*, 882–891. [CrossRef]
10. Al-Samman, T.; Li, X. Sheet Texture Modification in Magnesium-Based Alloys by Selective Rare Earth Alloying. *Mater. Sci. Eng. A* **2011**, *528*, 3809–3822. [CrossRef]
11. Patel, M.; Paudel, Y.; Mujahid, S.; Rhee, H.; El Kadiri, H. Self-Consistent Crystal Plasticity Modeling of Slip-Twin Interactions in Mg Alloys. *Crystals* **2023**, *13*, 653. [CrossRef]
12. Ishiguro, Y.; Huang, X.; Tsukada, Y.; Koyama, T.; Chino, Y. Effect of Bending and Tension Deformation on the Texture Evolution and Stretch Formability of Mg–Zn–RE–Zr Alloy. *Int. J. Miner. Metall. Mater.* **2022**, *29*, 1334. [CrossRef]
13. Griffits, D.; Davis, B.; Robson, J.D. The Influence of Strain Path on Rare Earth Recrystallization Textures in a Magnesium-Zinc-Rare Earth Alloy. *Metal. Mater. Trans. A* **2018**, *49*, 321–332. [CrossRef]
14. Habib, S.A.; Khan, A.S.; Gnäupel-Herold, T.; Lloyd, J.T.; Schoenfeld, S.E. Anisotropy, Tension-Compression Asymmetry and Texture Evolution of a Rare-Earth-Containing Magnesium Alloy Sheet, ZEK100, at Different Strain Rates and Temperatures: Experiments and Modeling. *Int. J. Plast.* **2017**, *95*, 163–190. [CrossRef]

15. Becker, R.; Lloyd, J.T. A Reduced-Order Crystal Model for HCP Metals: Application to Mg. *Mech. Mater.* **2016**, *98*, 98–110. [CrossRef]
16. Abedini, A.; Butcher, C.; Worswick, M.J. Experimental Fracture Characterisation of an Anisotropic Magnesium Alloy Sheet in Proportional and Non-proportional Loading Conditions. *Int. J. Solids Struct.* **2018**, *144–145*, 1–19. [CrossRef]
17. Abedini, A.; Butcher, C.; Worswick, M.J. Fracture Characterization of Rolled Sheet Alloys in Shear Loading: Studies of Specimen Geometry, Anisotropy, and Rate Sensitivity. *Exp. Mech.* **2017**, *57*, 75–88. [CrossRef]
18. Ray, A.K.; Wilkinson, D.S. The Effect of Microstructure on Damage and Fracture in AZ31B and ZEK100 Magnesium Alloys. *Mater. Sci. Eng. A* **2016**, *658*, 33–41. [CrossRef]
19. Omer, K.; Butcher, C.; Worswick, M. Characterization of Heat Transfer Coefficient for Non-isothermal Elevated Temperature Forming of Metal Alloys. *Int. J. Mater. Form.* **2020**, *13*, 177–201. [CrossRef]
20. Hadadzadeh, A.; Wells, M.A.; Javaid, A. Warm and Hot Deformation Behavior of As-Cast ZEK100 Magnesium Alloy. *Exp. Mech.* **2016**, *56*, 259–271. [CrossRef]
21. Min, J.; Hector, L.G., Jr.; Lin, J.; Carter, J.T.; Sachdev, A.K. Spatio-temporal Characteristics of Propagative Plastic Instabilities in a Rare Earth Containing Magnesium Alloy. *Int. J. Plast.* **2014**, *57*, 52–76. [CrossRef]
22. Li, Q.; Yea, W.; Gaoa, H.; Gao, L. Improving the Corrosion Resistance of ZEK100 Magnesium Alloy by Combining High-pressure Torsion Technology with Hydroxyapatite Coating. *Mater. Des.* **2019**, *181*, 107933. [CrossRef]
23. Kamrani, S.; Fleck, C. Effects of Calcium and Rare-earth Elements on the Microstructure and Tension–Compression Yield Asymmetry of ZEK100 Alloy. *Mater. Sci. Eng. A* **2014**, *618*, 238–243. [CrossRef]
24. Ertürk, S.; Brocks, W.; Bohlen, J.; Letzig, D.; Steglich, D. A Constitutive Law for the Thermo-mechanical Modelling of Magnesium Alloy Extrusion. *Int. J. Mater. Form.* **2012**, *5*, 325–339. [CrossRef]
25. Dobroň, P.; Chmelík, F.; Parfenenko, K.; Letzig, D.; Bohlen, J. On the Effect of the Extrusion Speed on Microstructure and Plastic Deformation of ZE10 and ZEK100 Magnesium Alloys—An Acoustic Emission Study. *Acta Phys. Pol.* **2012**, *122*, 593–596. [CrossRef]
26. Javaid, A.; Czerwinski, F. Effect of Hot Rolling on Microstructure and Properties of the ZEK100 Alloy. *J. Magn. Alloys* **2019**, *7*, 27–37. [CrossRef]
27. Boba, M.; Butcher, C.; Panahi, N.; Worswick, M.J.; Mishra, R.K.; Carter, J.T. Warm Forming Limits of Rare Earth-magnesium Alloy ZEK100 Sheet. *Int. J. Mater. Form.* **2017**, *10*, 181–191. [CrossRef]
28. Roostaei, A.A.; Ling, Y.; Jahed, H.; Glinka, G. Applications of Neuber's and Glinka's Notch Plasticity Correction Rules to Asymmetric Magnesium Alloys Under Cyclic Load. *Theor. Appl. Fract. Mech.* **2020**, *105*, 102431. [CrossRef]
29. Ling, Y.; Roostaei, A.A.; Glinka, G.; Jahed, H. Fatigue of ZEK100-F Magnesium Alloy: Characterisation and Modelling. *Int. J. Fatigue* **2019**, *125*, 179–186. [CrossRef]
30. Chen, G.; Ren, J.; Gao, H.; Cui, Y.; Chen, X. Pseudoelastic and Corrosion Behaviors of Mg ZEK100 Alloy under Cyclic Loading. *Int. J. Fatigue* **2017**, *103*, 466–477. [CrossRef]
31. Mokdad, F.; Chen, D.L. Cyclic Deformation and Anelastic Behavior of ZEK100 Magnesium Alloy: Effect of Strain Ratio. *Mater. Sci. Eng. A* **2015**, *640*, 243–258. [CrossRef]
32. Mokdad, F.; Chen, D.L. Strain-controlled Low Cycle Fatigue Properties of a Rare-earth Containing ZEK100 Magnesium Alloy. *Mater. Des.* **2015**, *67*, 436–447. [CrossRef]
33. Min, J.; Lin, J. Anelastic Behavior and Phenomenological Modeling of Mg ZEK100-O Alloy Sheet under Cyclic Tensile Loading–Unloading. *Mater. Sci. Eng. A* **2013**, *561*, 174–182. [CrossRef]
34. Noder, J.; Abedini, A.; Butcher, C. Evaluation of the VDA 238–100 Tight Radius Bend Test for Plane Strain Fracture Characterization of Automotive Sheet Metals. *Exp. Mech.* **2020**, *60*, 787–800. [CrossRef]
35. Aslam, I.; Li, B.; McClelland, Z.; Horstemeyer, S.J.; Maa, Q.; Wang, P.T.; Horstemeyer, M.F. Three-point Bending Behavior of a ZEK100 Mg Alloy at Room Temperature. *Mater. Sci. Eng. A* **2014**, *590*, 168–173. [CrossRef]
36. Min, J.; Lin, J.; Li, J. Forming Limits of Mg alloy ZEK100 Sheet in Preform Annealing Process. *Mater. Des.* **2014**, *53*, 947–953. [CrossRef]
37. Min, J.; Hector, L.G., Jr.; Lin, J.; Carter, J.T. Analytical Method for Forming Limit Diagram Prediction with Application to a Magnesium ZEK100-O Alloy. *J. Mater. Eng. Perform.* **2013**, *22*, 3324–3336. [CrossRef]
38. Antoniswamy, A.R.; Carpenter, A.J.; Carter, J.T.; Hector, L.G., Jr.; Taleff, E.M. Forming-Limit Diagrams for Magnesium AZ31B and ZEK100 Alloy Sheets at Elevated Temperatures. *J. Mater. Eng. Perform.* **2013**, *22*, 3389–3397. [CrossRef]
39. Paudel, Y.R.; Indeck, J.; Hazeli, K.; Priddy, M.W.; Inal, K.; Rhee, H.; Barrett, C.D.; Whittington, W.R.; Limmer, K.R.; El Kadiri, H. Characterization and Modeling of {1012} Twin Banding in Magnesium. *Acta Mater.* **2020**, *183*, 438–451. [CrossRef]
40. Bong, H.J.; Hu, X.; Sun, X.; Ren, Y. Temperature-dependent Constitutive Modeling of a Magnesium Alloy ZEK100 Sheet Using Crystal Plasticity Models Combined with in situ High-energy X-ray Diffraction Experiment. *J. Magnes. Alloys* **2022**, *10*, 2801–2816. [CrossRef]
41. Sun, X.; Zhang, B.; Jiang, Y.; Wu, P.; Wang, H. Multi-Island Genetic-Algorithm-Based Approach to Uniquely Calibrate Polycrystal Plasticity Models for Magnesium Alloys. *JOM* **2021**, *73*, 1395–1403. [CrossRef]
42. Bong, H.J.; Hu, X.; Sun, X.; Ren, Y. Mechanism-based Constitutive Modeling of ZEK100 Magnesium Alloy with Crystal Plasticity and in-situ HEXRD Experiment. *Int. J. Plast.* **2019**, *113*, 35–51. [CrossRef]

43. Abedini, A.; Butcher, C.; Worswick, M.J. Application of an Evolving Non-Associative Anisotropic-Asymmetric Plasticity Model for a Rare-Earth Magnesium Alloy. *Metals* **2018**, *8*, 1013. [CrossRef]
44. Zhang, K.; Badreddine, H.; Saanouni, K. Thermodynamically-Consistent Constitutive Modeling of Hardening Asymmetry Including Isotropic Ductile Damage for Mg Alloys. *Eur. J. Mech. A Solids* **2019**, *73*, 169–180. [CrossRef]
45. Abedini, A.; Butcher, C.; Nemcko, M.J.; Kurukuri, S.; Worswick, M.J. Constitutive Characterization of a Rare-Earth Magnesium Alloy Sheet (ZEK100-O) in Shear Loading: Studies of Anisotropy and Rate Sensitivity. *Int. J. Mech. Sci.* **2017**, *128–129*, 54–69. [CrossRef]
46. Muhammad, W.; Mohammadi, M.; Kang, J.; Mishra, R.K.; Inal, K. An Elasto-Plastic Constitutive Model for Evolving Asymmetric/anisotropic Hardening Behavior of AZ31B and ZEK100 Magnesium Alloy Sheets Considering Monotonic and Reverse Loading Paths. *Int. J. Plast.* **2015**, *70*, 30–59. [CrossRef]
47. Sharma, S.K.; Saxena, K.K.; Malik, V.; Mohammed, K.A.; Prakash, C.; Buddhi, D.; Dixit, S. Significance of Alloying Elements on the Mechanical Characteristics of Mg-Based Materials for Biomedical Applications. *Crystals* **2022**, *12*, 1138. [CrossRef]
48. Gao, H.; Zhang, M.; Zhao, J.; Gao, L.; Li, M. In Vitro and in Vivo Degradation and Mechanical Properties of ZEK100 Magnesium Alloy Coated with Alginate, Chitosan and Mechano-growth Factor. *Mater. Sci. Eng. C* **2016**, *63*, 450–461. [CrossRef] [PubMed]
49. Grillo, C.A.; Alvarez, F.; Fernández Lorenzo de Mele, M.A. Degradation of Bioabsorbable Mg-based Alloys: Assessment of the Effects of Insoluble Corrosion Products and Joint Effects of Alloying Components on Mammalian Cells. *Mater. Sci. Eng. C* **2016**, *58*, 372–380. [CrossRef] [PubMed]
50. Reifenrath, J.; Marten, A.-K.; Angrisani, N.; Eifler, R.; Weizbauer, A. In vitro and in vivo Corrosion of the Novel Magnesium Alloy Mg–La–Nd–Zr: Influence of the Measurement Technique and in vivo Implant Location. *Biomed. Mater.* **2015**, *10*, 045021. [CrossRef] [PubMed]
51. Zhao, J.; Gao, L.-L.; Gao, H.; Yuan, X.; Chen, X. Biodegradable Behaviour and Fatigue Life of ZEK100 Magnesium Alloy in Simulated Physiological Environment. *Fatigue Fract. Eng. Mater. Struct.* **2015**, *38*, 904–913. [CrossRef]
52. Bondarenko, A.; Angrisani, N.; Meyer-Lindenberg, A.; Seitz, J.M.; Waizy, H.; Reifenrath, J. Magnesium-based Bone Implants: Immunohistochemical Inalysis of Peri-implant Osteogenesis by Evaluation of Osteopontin and Osteocalcin Expression. *J. Biomed. Mater. Res. Part A* **2014**, *102*, 1449–1457. [CrossRef]
53. Weizbauer, A.; Modrejewski, C.; Behrens, S.; Klein, H.; Helmecke, P.; Seitz, J.-M.; Windhagen, H.; Möhwald, K.; Reifenrath, J.; Waizy, H. Comparative in vitro Study and Biomechanical Testing of Two Different Magnesium Alloys. *J. Biomater. Appl.* **2014**, *28*, 1264–1273. [CrossRef]
54. Dziuba, D.; Meyer-Lindenberg, A.; Seitz, J.M.; Waizy, H.; Angrisani, N.; Reifenrath, J. Long-term in vivo Degradation Behaviour and Biocompatibility of the Magnesium Alloy ZEK100 for use as a Biodegradable Bone Implant. *Acta Biomater.* **2013**, *9*, 8548–8560. [CrossRef]
55. Reifenrath, J.; Angrisani, N.; Erdmann, N.; Lucas, A.; Waizy, H.; Seitz, J.M.; Bondarenko, A.; Meyer-Lindenberg, A. Degrading Magnesium Screws ZEK100: Biomechanical Testing, Degradation Analysis and Soft-tissue Biocompatibility in a Rabbit Model. *Biomed. Mater.* **2013**, *8*, 045012. [CrossRef] [PubMed]
56. Bauer, M.; Biskup, C.; Schilling, T.; Haverich, A.; Bach, F.W.; Maier, H.J.; Hassel, T. Influence of Shot Peening on Surface Rougness and in vitro Load Cycles of Magnesium Alloys. *Biomed. Tech.* **2013**, *58*, 4060. [CrossRef]
57. Weidling, M.; Besdo, S.; Schilling, T.; Bauer, M.; Hassel, T.; Haverich, A.; Wriggers, P. Finite Element Simulation of Myocardial Stabilising Structures and Development of New Designs. *Biomed. Tech.* **2013**, *58*, 4061. [CrossRef] [PubMed]
58. Schulman, J.; Meyer-Lindenberg, A.; Goblet, F.; Bormann, D.; Stiller, W.; Seifert, H. Phantomuntersuchungen an einem Hochauflösenden CT zur Ex-vivo-Darstellung von Degradierbaren Magnesiumimplantaten und Simulierten Periimplantären Knochenschichten in Kaninchentibiae. *Fortschr. Röntgenstr.* **2012**, *184*, 455–460. [CrossRef] [PubMed]
59. Huehnerschulte, T.A.; Angrisani, N.; Rittershaus, D.; Bormann, D.; Windhagen, H.; Meyer-Lindenberg, A. In Vivo Corrosion of Two Novel Magnesium Alloys ZEK100 and AX30 and Their Mechanical Suitability as Biodegradable Implants. *Materials* **2011**, *4*, 1144–1167. [CrossRef] [PubMed]
60. Huehnerschulte, T.A.; Reifenrath, J.; von Rechenberg, B.; Dziuba, D.; Seitz, J.M.; Bormann, D.; Windhagen, H.; Meyer-Lindenberg, A. In vivo Assessment of the Host Reactions to the Biodegradation of the Two Novel Magnesium Alloys ZEK100 and AX30 in an Animal Model. *BioMed. Eng. OnLine* **2012**, *11*, 14. [CrossRef]
61. Seitz, J.-M.; Utermöhlen, D.; Wulf, E.; Klose, C.; Bach, F.-W. The Manufacture of Resorbable Suture Material from Magnesium—Drawing and Stranding of Thin Wires. *Adv. Eng. Mater.* **2011**, *13*, 1087–1095. [CrossRef]
62. Seitz, J.-M.; Wulf, E.; Freytag, P.; Bormann, D.; Bach, F.-W. The Manufacture of Resorbable Suture Material from Magnesium. *Adv. Eng. Mater.* **2010**, *12*, 1099–1105. [CrossRef]
63. Gao, H.; Ye, W.; Zhang, Z.; Gao, L. Ratcheting Behavior of ZEK100 Magnesium Alloy with Various Loading Conditions and Different Immersing Time. *J. Mater. Res.* **2017**, *32*, 2143–2152. [CrossRef]
64. Zaghloul, B.; Kish, J.R. Corrosion Inhibition of Mg Alloy ZEK100 Sheet Metal by Dissolved Lithium Carbonate. *J. Electrochem. Soc.* **2021**, *168*, 081507. [CrossRef]
65. Brady, M.P.; Rother, G.; Frith, M.G.; Ievlev, A.E.; Leonard, D.N.; Littrell, K.C.; Cakmak, E.; Meyer, H.M., III; Anovitz, L.M.; Davis, B. Temporal Evolution of Corrosion Film Nano-Porosity and Magnesium Alloy Hydrogen Penetration in NaCl Solution. *J. Electrochem. Soc.* **2020**, *167*, 131513. [CrossRef]

66. Brady, M.P.; Leonard, D.N.; McNally, E.A.; Kish, J.R.; Meyer, H.M.; Cakmak, E.; Davis, B. Magnesium Alloy Effects on Plasma Electrolytic Oxidation Electro-Ceramic and Electro-Coat Formation and Corrosion Resistance. *J. Electrochem. Soc.* **2019**, *166*, C492–C508. [CrossRef]
67. Binns, W.J.; Zargarzadah, F.; Dehnavi, V.; Chen, J.; Noël, J.J.; Shoesmith, D.W. Physical and Electrochemical Evidence for the Role of a Mg Hydride Species in Mg Alloy Corrosion. *Corrosion* **2019**, *75*, 58–68. [CrossRef]
68. Brady, M.P.; Leonard, D.N.; Meyer, H.M., III; Thomson, J.K.; Unocic, K.A.; Elsentriecy, H.H.; Song, G.-L.; Kitchen, K.; Davis, B. Advanced Characterization Study of Commercial Conversion and Electrocoating Structures on Magnesium Alloys AZ31B and ZE10A. *Surf. Coat. Technol.* **2016**, *294*, 164–176. [CrossRef]
69. Dauphin-Ducharme, P.; Binns, W.J.; Snowden, M.E.; Shoesmith, D.W.; Mauzeroll, J. Determination of the Local Corrosion Rate of Magnesium Alloys Using a Shear Force Mounted Scanning Microcapillary Method. *Faraday Discuss.* **2015**, *180*, 331–345. [CrossRef]
70. Asmussen, R.M.; Binns, W.J.; Jakupi, P.; Shoesmith, D. The Influence of Microstructure on the Corrosion of Magnesium Alloy ZEK100. *Corrosion* **2015**, *71*, 242–254. [CrossRef]
71. Waizy, H.; Weizbauer, A.; Modrejewski, C.; Witte, F.; Windhagen, H.; Lucas, A.; Kieke, M.; Denken, B.; Behrens, P.; Meyer-Lindenberg, A.; et al. In vitro Corrosion of ZEK100 Plates in Hank's Balanced Salt Solution. *BioMed Eng. Online* **2012**, *11*, 12. [CrossRef] [PubMed]
72. Bauer, M.; Hassel, T.; Biskup, C.; Hartung, D.; Schilling, T.; Weidling, M.; Wriggers, P.; Wacker, F.; Bach, F.W.; Haverich, A. Geometric Adaption of Resorbable Myocardial Stabilizing Structures Based on the Magnesium Alloys LA63 and ZEK100 for the Support of Myocardial Grafts on the Left Ventricle. *Biomed. Eng.* **2012**, *57*, 22–25. [CrossRef]
73. Krüger, R.; Seitz, J.-M.; Ewald, A.; Bach, F.-W.; Groll, J. Strong and Tough Magnesium Wire Reinforced Phosphate Cement Composites for Load-bearing Bone Replacement. *J. Mech. Behav. Biomed. Mater.* **2013**, *20*, 36–44. [CrossRef] [PubMed]
74. Peng, H.; Chen, D.L.; Bai, X.F.; Wang, P.Q.; Li, D.Y.; Jiang, X.Q. Microstructure and Mechanical Properties of Mg-to-Al Dissimilar Welded Joints with an Ag Interlayer using Ultrasonic Spot Welding. *J. Magn. Alloys* **2020**, *8*, 552–563. [CrossRef]
75. Peng, H.; Chen, D.L.; Bai, X.F.; She, X.W.; Li, D.Y.; Jiang, X.Q. Ultrasonic Spot Welding of Magnesium-to-Aluminum Alloys with a Copper Interlayer: Microstructural Evolution and Tensile Properties. *J. Manuf. Proc.* **2019**, *37*, 91–100. [CrossRef]
76. Peng, H.; Jiang, X.; Bai, X.; Li, D.; Chen, D. Microstructure and Mechanical Properties of Ultrasonic Spot Welded Mg/Al Alloy Dissimilar Joints. *Metals* **2018**, *8*, 229. [CrossRef]
77. Macwan, A.; Chen, D.L. Ultrasonic Spot Welding of Rare-Earth Containing ZEK100 Magnesium Alloy to 5754 Aluminum Alloy. *Mater. Sci. Eng. A* **2016**, *666*, 139–148. [CrossRef]
78. Macwan, A.; Chen, D.L. Ultrasonic Spot Welding of a Rare-Earth Containing ZEK100 Magnesium Alloy: Effect of Welding Energy. *Metal. Mater Trans. A* **2016**, *47*, 1686–1697. [CrossRef]
79. Chen, Y.; Chen, J.; Amirkhiz, B.S.; Worswick, M.J.; Gerlich, A.P. Microstructures and Properties of Mg alloy/DP600 Steel Dissimilar Refill Friction Stir Spot Welds. *Sci. Technol. Weld. Join.* **2015**, *20*, 494–501. [CrossRef]
80. Rodriguez, R.I.; Jordon, J.B.; Rao, H.M.; Badarinarayan, H.; Yuan, W.; ElKadiri, H.; Allison, P.G. Microstructure, Texture, and Mechanical Properties of Friction Stir Spot Welded Rare-Earth Containing ZEK100 Magnesium Alloy Sheets. *Mater. Sci. Eng. A* **2014**, *618*, 637–644. [CrossRef]
81. Yang, J.; Yu, Z.; Li, Y.; Zhang, H.; Zhou, N. Laser Welding/Brazing of 5182 Aluminium Alloy to ZEK100 Magnesium Alloy Using a Nickel Interlayer. *Sci. Technol. Weld. Join.* **2018**, *23*, 543–550. [CrossRef]
82. Yang, J.; Su, J.H.; Yu, Z.S.; Zhang, G.Z.; Lin, S.B.; Li, Y.L.; Zhou, N.Y. Influence of Ni Interlayer Width on Interfacial Reactions and Mechanical Properties in Laser Welding/Brazing of Al/Mg Lap Joint. *Sci. Technol. Weld. Join.* **2019**, *25*, 37–44. [CrossRef]
83. Kuang, J.; Li, X.; Ye, X.; Tang, J.; Liu, H.; Wang, J.; Tang, G. Microstructure and Texture Evolution of Magnesium Alloys During Electropulse Treatment. *Metall. Mater. Trans. A* **2015**, *46*, 1789–1804. [CrossRef]
84. Cahn, J.W. Critical Point Wetting. *J. Chem. Phys.* **2008**, *66*, 3667. [CrossRef]
85. Ebner, C.; Saam, W.F. New Phase-Transition Phenomena in Thin Argon Films. *Phys. Rev. Lett.* **1977**, *38*, 1486. [CrossRef]
86. Straumal, B.B.; Polyakov, S.A.; Bischoff, E.; Gust, W.; Mittemeijer, E.J. Faceting of Σ3 and Σ9 grain boundaries in copper. *Interface Sci.* **2001**, *9*, 287–292. [CrossRef]
87. Maksimova, E.L.; Shvindlerman, L.S.; Straumal, B.B. Transformation of Σ17 special tilt boundaries to general boundaries in tin. *Acta Metall.* **1988**, *36*, 1573–1583. [CrossRef]
88. Laporte, D.; Watson, E.B. Experimental and Theoretical Constraints on Melt Distribution in Crustal Sources: The Effect of Crystalline Anisotropy on Melt Interconnectivity. *Chem. Geol.* **1995**, *124*, 161–184. [CrossRef]
89. Noskovich, O.I.; Rabkin, E.I.; Semenov, V.N.; Straumal, B.B.; Shvindlerman, L.S. Wetting and premelting phase transitions in 38°[100] tilt grain boundaries in (Fe–12at.%Si) Zn alloy in the vicinity of the A2–B2 bulk ordering in Fe–12at.%Si alloy. *Acta Metall. Mater.* **1991**, *39*, 3091–3098. [CrossRef]
90. Chang, L.-S.; Rabkin, E.; Straumal, B.B.; Hoffmann, S.; Baretzky, B.; Gust, W. Grain boundary segregation in the Cu–Bi system. *Defect Diff. Forum* **1998**, *156*, 135–146. [CrossRef]
91. Ross, D.; Bonn, D.; Meunier, J. Observation of Short-Range Critical Wetting. *Nature* **1999**, *400*, 737–739. [CrossRef]
92. Straumal, B.B.; Gust, W.; Watanabe, T. Tie lines of the grain boundary wetting phase transition in the Zn-rich part of the Zn–Sn phase diagram. *Mater. Sci. Forum* **1999**, *294–296*, 411–414. [CrossRef]
93. German, R.M.; Suri, P.; Park, S.J. Review: Liquid Phase Sintering. *J. Mater. Sci.* **2009**, *44*, 1–39. [CrossRef]

94. Rabkin, E.I.; Shvindlerman, L.S.; Straumal, B.B. Grain Boundaries: Phase Transitions and Critical Phenomena. *Int. J. Mod. Phys. B* **1991**, *5*, 2989–3028. [CrossRef]
95. Straumal, B.; Rabkin, E.; Lojkowski, W.; Gust, W.; Shvindlerman, L.S. Pressure influence on the grain boundary wetting phase transition in Fe–Si alloys. *Acta Mater.* **1997**, *45*, 1931–1940. [CrossRef]
96. Straumal, A.B.; Mazilkin, I.A.; Tsoi, K.V.; Baretzky, B.; Straumal, B.B. "Wetting" Phase Transitions by the Second Solid Phase for Linear Defects (Grain Boundary Triple Junctions). *JETP Lett.* **2020**, *112*, 257–261. [CrossRef]
97. Straumal, A.B.; Bokstein, B.S.; Petelin, A.L.; Straumal, B.B.; Baretzky, B.; Rodin, A.O.; Nekrasov, A.N. Apparently Complete Grain Boundary Wetting in Cu–In Alloys. *J. Mater. Sci.* **2012**, *47*, 8336–8343. [CrossRef]
98. Jandaghi, M.R.; Pouraliakbar, H.; Hong, S.I.; Pavese, M. Grain Boundary Transition Associated Intergranular Failure Analysis at TMAZ/SZ Interface of Dissimilar AA7475-AA2198 Joints by Friction Stir Welding. *Mater. Lett.* **2020**, *280*, 128557. [CrossRef]
99. Jandaghi, M.R.; Pouraliakbar, H.; Saboori, A.; Hong, S.I.; Pavese, M. Comparative Insight into the Interfacial Phase Evolutions during Solution Treatment of Dissimilar Friction Stir Welded AA2198-AA7475 and AA2198-AA6013 Aluminum Sheets. *Materials* **2021**, *14*, 1290. [CrossRef]
100. Straumal, B.B.; Kogtenkova, O.; Zięba, P. Wetting Transition of Grain Boundary Triple Junctions. *Acta Mater.* **2008**, *56*, 925–933. [CrossRef]
101. Cantwell, P.R.; Tang, M.; Dillon, S.J.; Luo, J.; Rohrer, G.S.; Harmer, M.P. Grain Boundary Complexions. *Acta Mater.* **2014**, *62*, 1–48. [CrossRef]
102. Straumal, B.B.; Mazilkin, A.A.; Protasova, S.G.; Schütz, G.; Straumal, A.B.; Baretzky, B. Observation of Pseudopartial Grain Boundary Wetting in the NdFeB-Based Alloy. *J. Mater. Eng. Perform.* **2016**, *25*, 3303–3309. [CrossRef]
103. Straumal, B.B.; Mazilkin, A.A.; Protasova, S.G.; Gusak, A.M.; Bulatov, M.F.; Straumal, A.B.; Baretzky, B. Grain Boundary Phenomena in NdFeB-Based Hard Magnetic Alloys. *Rev. Adv. Mater. Sci.* **2014**, *38*, 17–28.
104. Straumal, B.B.; Rodin, A.O.; Shotanov, A.E.; Straumal, A.B.; Kogtenkova, O.A.; Baretzky, B. Pseudopartial Grain Boundary Wetting: Key to the Thin Intergranular Layers. In *Defect and Diffusion Forum*; Trans Tech Publications Ltd.: Wollerau, Switzerland, 2013; Volume 333, pp. 175–192. [CrossRef]
105. Straumal, B.B.; Mazilkin, A.A.; Sauvage, X.; Valiev, R.Z.; Straumal, A.B.; Gusak, A.M. Pseudopartial Wetting of Grain Boundaries in Severely Deformed Al-Zn Alloys. *Russ. J. Non-Ferr. Met.* **2015**, *56*, 44–51. [CrossRef]
106. Langenohl, L.; Brink, T.; Richter, G.; Dehm, G.; Liebscher, C.H. Atomic-resolution observations of silver segregation in a [111] tilt grain boundary in copper. *Phys. Rev. B* **2023**, *107*, 134112. [CrossRef]
107. Bishara, H.; Langenohl, L.; Zhou, X.; Gault, B.; Best, J.P.; Dehm, G. Decoupling the Electrical Resistivity Contribution of Grain Boundaries in Dilute Fe-alloyed Cu Thin Films. *Scr. Mater.* **2023**, *230*, 115393. [CrossRef]
108. Brink, T.; Langenohl, L.; Bishara, H.; Dehm, G. Universality of Grain Boundary Phases in fcc metals: Case Study on High-Angle [111] Symmetric Tilt Grain Boundaries. *Phys. Rev. B* **2023**, *107*, 054103. [CrossRef]